Available online at www.sciencedirect.com

jmr&t Journal of Materials Research and Technology

www.jmrt.com.br

Original Article

Improvement of formability and tensile mechanical properties of SAE 970X steel by controlled rolling process

Mohammad Masoumi[a,b,*], *Edwan Anderson Ariza Echeverri*[a,c], *Cleiton Carvalho Silva*[d], *Willys Machado Aguiar*[d], *Hamilton Ferreira Gomes de Abreu*[d]

[a] *Universidade de São Paulo (USP), Departamento de Engenharia Metalúrgica e de Materiais da Escola Politécnica, Av. Professor Mello Moraes, 2463, CEP: 05508-030, São Paulo, SP, Brazil*

[b] *Universidade Federal do ABC, Centro de Engenharia, Modelagem e Ciências Sociais Aplicadas, Bangú, 09210-580, Santo André, SP, Brazil*

[c] *Mechanical Technology Program, Technological University of Pereira, Vereda La Julita, Pereira, Risaralda, Colombia*

[d] *Universidade Federal do Ceará (UFC), Departamento de Engenharia e Ciência de Materiais, Campus do Pici, Bloco 729 CEP: 60440-554, Fortaleza, CE, Brazil*

ARTICLE INFO

Article history:
Received 27 November 2017
Accepted 11 June 2018
Available online 23 November 2018

Keywords:
Texture
Electron backscattered diffraction
Tensile properties
Erichsen test

ABSTRACT

It is believed that texture, as the preferred crystallographic orientation of microstructural features, causes plastic anisotropy, leading to a decrease in formability. Thus, promoting recrystallization and randomizing crystallographic texture have been the main methods of increasing formability. The aim of the current study was to improve the tensile properties and formability by means of controlling the microstructural features under controlled rolling processes in an SAE 970X steel. The evolution of microstructure, crystallographic orientation, and grain boundary distribution was analyzed by scanning electron microscope, X-ray diffraction, and electron backscatter diffraction. The results of tensile uniaxial tests and equibiaxial tension behaviors showed that the ultrafine ferrite grains oriented along the {011} and {111} planes parallel to the rolling direction, with adequate slip systems accompanied by the dispersion of martensite/austenite (M–A) microconstituents in the ferritic structure, improved the tensile mechanical properties and formability. The sample subjected to isothermal rolling at 850 °C achieved successful results compared to as-received and other controlled rolling methods.

1. Introduction

Society of Automotive Engineers (SAE) indicates that steels are widely used in heavy-duty highway engines (or truck applications or tractor-trailers) and off-road vehicles, mining

* *Corresponding author.*
E-mail: mohammad.masoumi@usp.br (M. Masoumi).

https://doi.org/10.1016/j.jmrt.2018.06.024

equipment, railroad cars, barges and dredges, snowmobiles, lawn mowers, and passenger car components [1,2]. For many engineering applications, favorable high strength-to-weight ratios, thickness reduction, formability, and weldability are steel requirements. Therefore, the higher yield strengths of SAE steels (higher grades than SAE 950X, e.g. 960X, 970X, 980X, etc.) are produced with a fine ferrite grain size formed during controlled hot rolling and precipitation strengthening due to the presence of vanadium, niobium, and titanium [3,4]. The purpose of these microalloyed steels is to increase load-carrying ability without increasing the carbon and/or manganese contents. However, the non-uniform deformation and early fracture of these steel grades are critical problems in engineering applications [5,6]. The effect of vanadium and niobium additions on strengthening by forming fine precipitate particles (such as niobium carbide or carbonitride) in the ferrite microstructure during cooling after hot rolling has been studied in detail [3,4,7].

Grain refinement (Hall–Petch effect) and precipitation strengthening have been proven to be the main hardening mechanisms (i.e. solid solution strengthening, precipitation hardening, and grain boundary strengthening) in low alloy and Nb/V microalloyed steels. Microalloyed steels with low carbon content (0.05–0.25 wt.%) and low alloying elements (less than wt.5%) exhibit superior mechanical properties and toughness because of the strengthening effects of niobium and vanadium [8–10]. Fine precipitates of niobium carbides and vanadium carbonitrides, formed at prior-austenite grain boundaries, restrict austenite grain growth during hot rolling, leading to a fine ferritic structure. As consequence, the formation of finer ferrite grain size from the fine prior-austenite grains simultaneously increases yield strength, toughness, and ductility. Mechanical property test data confirmed a significant increase in strength and hardness by refinement of the ferrite structure. Besides, the ductility of the investigated steels can be improved thanks to the application of annealing, which turns the deformation-induced substructure into stable ultra-fine grains [11,12]. Moreover, the fine-grained materials containing a large amount of dislocations and strain-induced boundaries formed through the accumulation and rearrangement of dislocation during the manufacturing processing, have two opposite effects [13–15]. On the one hand, the high dislocation densities lead to higher strength and hardness due to the barriers impeding sliding by decreasing the grain size. Conversely, dislocation-trapping effects that occur extensively at grain boundaries reduce dislocation interaction and consequently reduce the strain-hardening capacity by leading to early localized deformation [16].

In addition, it is well known that the crystallographic textures developed by manufacturing processing and post-heat treatments play a significant role in the mechanical properties. The specific grain orientation shows different yield stress response as a function of strain in the selected load direction (i.e., anisotropy) [11–13]. Recently, Blondé et al. [17] and Sainath et al. [18,19] analyzed the lattice plane strains of grains for specific $\{hkl\}$ planes oriented with the plane normal along the tensile direction. They showed the gradual evolution of interplanar spacing (d-spacing) with changes in Young's modulus and yield strength. For instance, {110} and {112} grains laid on the closest close-packed planes with low inter-atomic distances in the body-centered cubic (BCC) structure show the highest yield stress. In contrast, dislocation gliding is restricted in {001} grains with a lack of adequate slip systems, with the largest interatomic spacing resulting in the least formability. Moreover, Ghosh et al. [20] reported that the presence of cleavage planes oriented along the {001} direction provides easy crack propagation, which may cause a decrease in the mechanical properties and the formability limits.

Numerous studies [8–10,21,7,22] have been conducted to explain the formation mechanism of (Ti, Nb, V) nanometric precipitates and its effects (such as size, fraction, and distribution) on mechanical properties. In this study, a commercial SAE 970X microalloyed steel was subjected to different controlled rolling processes followed by air cooling to room temperature. The main idea is to propose a novel rolling process for improving the tensile mechanical properties and formability by controlling the microstructure and crystallographic texture (i.e., grain orientation, low and high angle boundaries). The evolution of the microstructure, crystallographic orientation, and grain boundary distribution was analyzed by scanning electron microscopy (SEM), X-ray diffraction (XRD), and electron backscatter diffraction (EBSD). Additionally, uniaxial tensile tests and biaxial tension tests (Erichsen test) were employed to propose a new rolling process.

2. Experimental procedures

A commercial SAE 970X steel plate, which was industrially hot-rolled after casting, was investigated. The chemical composition was determined by optical emission spectrometry (Shimadzu, PDA-7000); see Table 1. Firstly, the samples were annealed at 1200 °C for one hour to obtain a homogenous austenitic microstructure and temperature distribution. Then, three rolling passes (15 mm → 11 mm → 8 mm → 5 mm) were applied to the specimens with different start and finish rolling temperatures, as shown in Fig. 1 and Table 2. After the finish rolling temperature, the samples were air cooled to room temperature. Rolling was conducted by a Stanat model TA-315 rolling machine with a rotational speed of 27 rpm and strain rates during each pass of approximately 3.5, 4.6, and 7.8 s^{-1}, respectively. Temperature tracking during the rolling operation was carried out by Minolta/Land Cyclops 152. The purpose of selecting a wide range of start and finish rolling temperatures – from a temperature higher than the non-recrystallization temperature (T_{NR} = 1006 °C [23]) to below the Ar_3 transformation temperature (737 °C [24]) in the intercritical ($\alpha+\gamma$) field – was to explore the effects of the evolution of the microstructure and crystal orientation during dynamic recrystallization and ferrite transformation on the final mechanical properties.

The microstructures in the longitudinal cross-section, that is, the section normal to the transverse direction (TD) and parallel to the rolling direction, were studied by SEM (FEI Quanta 450 FEG) operated at a nominal voltage of 20 kV. The specimens were ground using silicon carbide paper with a grit size from 100 to 1200, followed by mechanical polishing with diamond paste (6, 3, and 1 μm) and etching in Nital 2% for approximately

Table 1 – Chemical composition of SAE 970X steel (wt.%) obtained by the emission spectrometry technique.

C	Si	Mn	S	Al	Cu	Cr	P	Ni	Mo	Nb	Ti	V
0.099	0.26	1.664	0.005	0.08	0.014	0.021	0.018	0.022	0.816	0.061	0.02	0.050

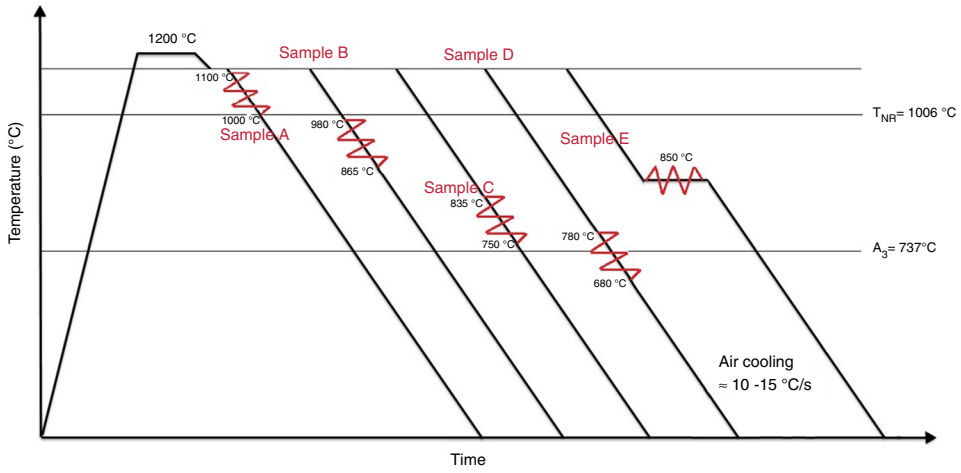

Fig. 1 – Schematic representation of the thermomechanical rolling processes with different start and finish rolling temperatures.

Table 2 – Thermomechanical schedules applied in the present study. FRT refers to the finish rolling temperatures (±20 °C).

Sample	Initial thickness (mm)	Start rolling temperature (°C)	Step one		Step two		Step three	
			Thickness (mm)	FRT (°C)	Thickness (mm)	FRT (°C)	Thickness (mm)	FRT (°C)
A		1100 ± 20		1060 ± 20		1040 ± 20		1000 ± 20
B		980 ± 20		955 ± 20		905 ± 20		865 ± 20
C	15 ± 0.05	835 ± 20	11 ± 0.05	795 ± 20	8 ± 0.05	785 ± 20	5 ± 0.05	750 ± 20
D		780 ± 20		720 ± 20		700 ± 20		680 ± 20
E		850 ± 20		850 ± 20		850 ± 20		850 ± 20

20 s. In addition, EBSD analysis was carried out using an HKL Channel 5 system attached to the SEM-FEI Quanta 450 FEG, with a tilt angle of 70°, step size of 0.5 μm, and working distances of 14–16 mm. To obtain a good quality of the Kikuchi diffraction patterns, the unetched polished SEM samples were polished for 3 h using 0.5 μm colloidal silica. The acquired data were post-processed with Channel 5 software and the MTEX free and open source software toolbox [25].

Macrotexture measurements were carried out using a Panalytical X-Pert texture goniometer equipped with monochromatic Cu Kα radiation. After identifying the exact peak positions via a θ–2θ scan, three {111}, {200}, and {220} incomplete ($\alpha = 0$–$85°$, $\beta = 0$–$360°$) pole figures of ferrite phase were collected at 5° intervals in step mode (counting time of 5 s/step). The crystalline orientation distribution function (ODF) of each sample was calculated from the measured pole figures using MTEX with cubic-orthorhombic symmetry. The distributed crystallographic orientation was measured using the MTEX algorithms by means of ordinary statistics, neglecting their spatial reference [26]. The related ODFs were plotted at constant $Q_2 = 45°$, which can present the most important crystal orientations according to the Bunge convention [27].

Vickers microhardness, uniaxial tensile, and Erichsen tests were conducted at room temperature to characterize mechanical behavior. Vickers microhardness test was carried out along the mid-thickness of specimens with a loading force of 4.903 N ($HV_{0.5}$) and a dwell time of 15 s using a Shimadzu HMV-2000, based on the ASTM E-384-08 standard. The average value was determined from ten indents in each sample. Tensile tests were carried out on an ADMET-eXpert 2600 machine, based on the ASTM E8M-13a standard, on samples with a gauge length of 50 mm and overall length of 200 mm along the rolling direction under an engineering strain rate of $2 \times 10^{-2}\,s^{-1}$ at room temperature. The average value of tensile mechanical properties was made from three uniaxial tensile tests for each condition. Furthermore, the stretch formability of the samples was evaluated using the Erichsen test (Erichsen Model 100 machine) according to the ISO 20482 standard. Erichsen samples with dimensions of 7 cm × 7 cm × 5 mm were sectioned from the rolling plane. The tests were performed at room temperature using a hemispherical punch with a diameter of 4 cm and testing velocity of $0.01\,mm\,s^{-1}$ using grease lubrication. The tests were performed until fracture of the sheets occurred. The Erichsen index (Ei) was evaluated from the

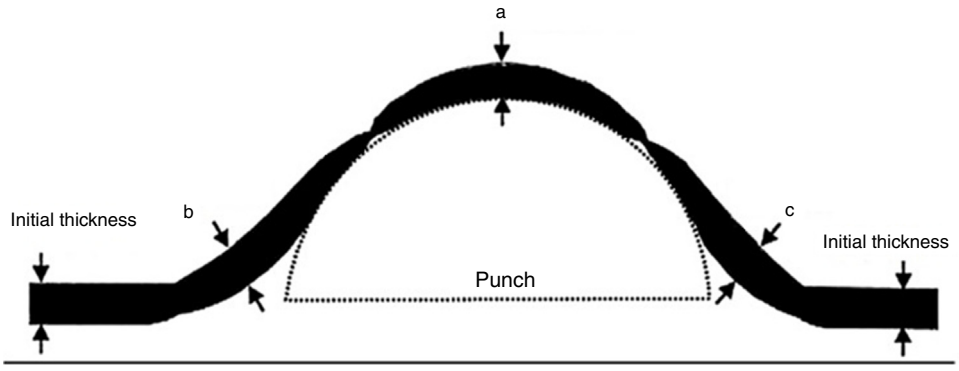

Fig. 2 – Appearance of dome free surfaces and cross-sections of Erichsen tested samples.

displacement obtained during the Erichsen tests. After Erichsen testing, each cup was sectioned along the dome centerline in the rolling direction and then placed on a flatbed scanner to take an image of the section, as shown in Fig. 2. Subsequently, the thickness profile was determined using the KLONK image measurement software tool. The maximum thickness of the sidewall (regions 'b' and 'c', in Fig. 2) indicates the limit of uniform deformation. Region 'a' also represents the minimum uniform deformation located at the top of the dome [28,29]. The measurement errors demonstrated by the thickness variation along the cross-section are associated with the forming variables, vertical location, sidewall effects, anisotropy, and sectioning variables.

3. Results and discussion

3.1. *SEM studies*

Fig. 3 presents the SEM micrographs of the investigated specimens. The as-received sample and sample A, which was finish-rolled in the austenite phase at recrystallization region, showed mainly polygonal ferrite and pearlite in the microstructure. A mixed microstructure containing granular bainite, acicular ferrite, degenerated pearlite, and small martensite/austenite (M–A) constituents was characterized in samples B and C, which were rolled in the intercritical ($\alpha+\gamma$) region (between Ar_3 and Ar_1). The sample rolled isothermally at 850 °C (sample E) also showed a uniform distribution of M–A constituents in bainite–ferrite microstructure. M–A constituents, ferrite, and pearlite resulted from the phase transformation of austenite during slow cooling in air to room temperature. Additionally, the pre-strain can accelerate the diffusional transformations due to the increase in the nucleation rate caused by the higher density of nucleation sites introduced. Carbon enrichment of the remaining austenite also occurs due to the nucleation and growth of the proeutectoid ferrite, since the carbon has low solubility in ferrite and high solubility in austenite. The blocky M–A constituents, or remaining austenite coexisting together with high carbon martensite, are formed under favorable conditions of chemical composition (high manganese content) and appropriate continuous cooling rates (air cooling to room temperature). Carbon is enriched in the untransformed austenite by carbon partitioning from ferrite into the remaining austenite during the austenitic decomposition [30,31], leading to the formation of a mixture of untempered martensite and austenite (M–A) constituent upon cooling. Sample D, which was finish-rolled at ≈680 °C in the single ferrite phase region, below the Ar_3 temperature, had elongated ferrite (Fig. 3e). Since the advancing α/γ interface is enriched in carbon by the partitioning, it is believed that the Fe_3C nucleation takes place at the interface boundary. In general, with the increase in the start rolling temperature, the cementite in pearlite changes from lamellar pearlite to degenerated pearlite [31]. The aggregation of ferrite layers and carbides (Fe_3C) in this sample can be classified as degenerate pearlite, leading to an improvement of the toughness [32]. Austenite can drag carbon and manganese atoms rejected from proeutectoid ferrite (equiaxed ferrite) and remains stable even below the Ar_3 temperature. Thus, the presence of M–A constituents can be explained by the delay of the pearlitic reaction below Ar_3 during the continuous cooling due to the high carbon and manganese contents in retained austenite.

In the studied steel, the presence of precipitates such as niobium and vanadium is beneficial for achieving fine-grained ferrite. The formation of fine ferrite grain sizes (less than 8 μm) was observed in all thermomechanically processed samples. The grain refinement results in improved toughness and higher yield strengths. Vanadium and niobium contribute to precipitation strengthening by forming fine precipitate particles (5–100 nm in diameter) in ferrite during cooling after hot rolling [5,33]. Also, this microalloying decreases the austenite-to-ferrite transformation temperature, leading to the formation of finer austenite grain sizes prior to transformation. The Vickers hardness was 172 ± 4 HV in the as-received steel and increased to 186 ± 5, 215 ± 5, 232 ± 7, 228 ± 4, and 218 ± 3 $HV_{0.5}$ in samples A to E, respectively. This hardness increase is associated with the effects of the random boundaries in ultra-fine grain sizes, which hinder the dislocation movements. The ultra-fine grains decrease the possibility of both dislocation–dislocation and dislocation–boundary interactions [34,35]. During the controlled rolling process analyzed, the austenite grain size of hot-rolled steels can be determined by the recrystallization and grain growth of austenite. The microscopic analysis

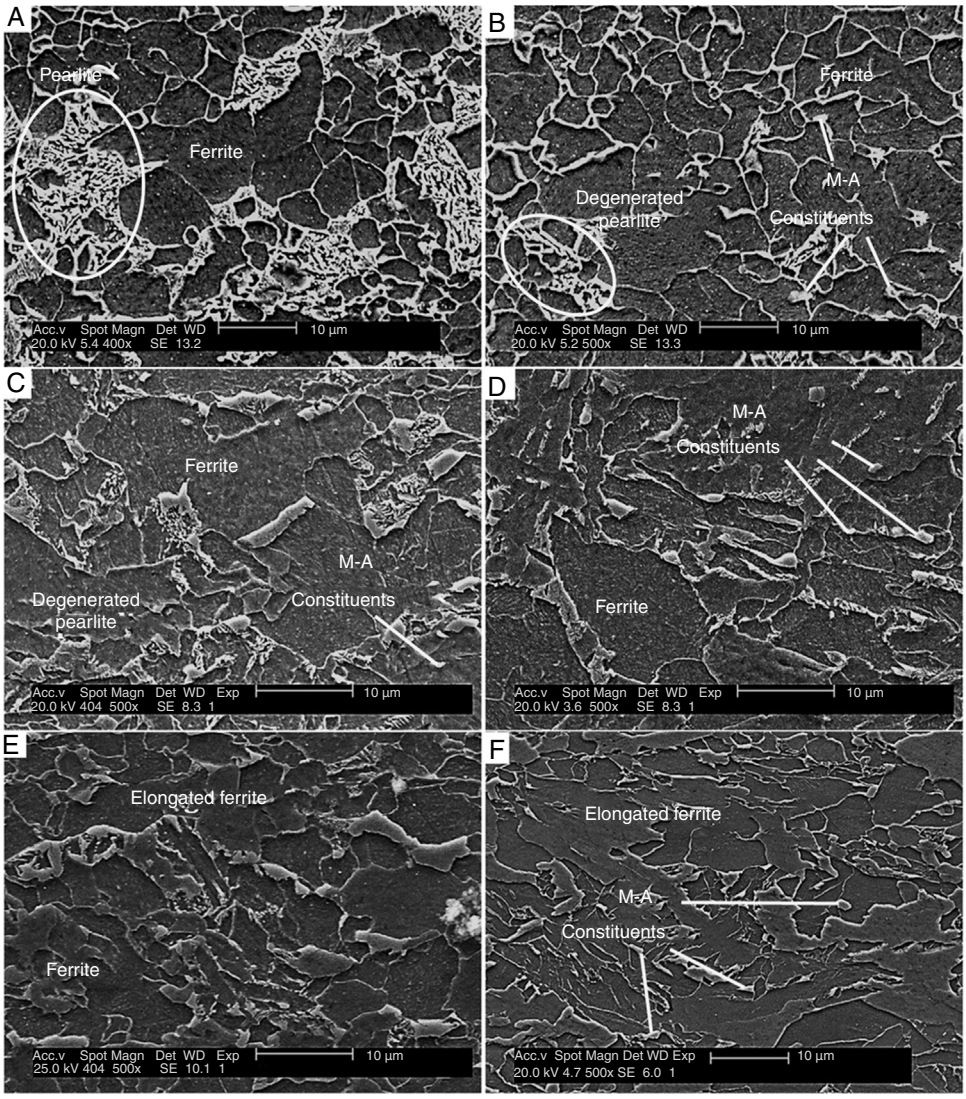

Fig. 3 – SEM micrographs of investigated specimens: (a) as-received; (b)–(f) samples A to E, respectively.

showed that the controlled rolling could control the final mechanical properties by precipitation hardening and grain boundary strengthening.

Temperature raises the carbon diffusion coefficient and increases the effective carbon diffusion distance in austenite [36]. On the one hand, proeutectoid ferrite forms from the austenite with very low carbon content. Deformation-induced ferrite transformation (DIFT effect) could be accelerated via control rolling processing. On the other hand, a limited carbon enrichment of remaining austenite develops due to the local conditions of carbon partitioning and increasing of carbon solubility in remaining austenite. Silva et al. [31] studied the morphological aspects and their correlation on the microhardness values. They showed that ferrite microhardness can be varied from 175 to 325 HV, because of its carbon content. Moreover, the microhardness of M–A constituents was determined to be about 400–680 HV in API X80 steel. In addition, Bhadeshia [37] documented that M–A constituents include the proportions of martensite and austenite, containing carbon concentration greater than its solubility in ferrite, from 0.6 up to 2.2 wt.% independently of steel carbon content [38,39]. Therefore, according to the kinetic conditions (time for carbon enrichment and ferrite growth), it is expected that the fraction of M–A would decrease with the decrease in deformation temperature. This could be explained by the stabilization of M–A through the carbon and manganese partitioning into the remaining austenite during cooling.

You et al. [40] documented that M–A constituents can be identified as non-transformed austenite Kikuchi patterns with satisfying Kurdjumov–Sachs orientation relationship. To verify the presence of M–A constituents or remaining austenite coexisting with martensite, EBSD analyses were carried out. However, although EBSD is a powerful technique for phase identification, it has some limitations such as in the detection of minority phases and quality of diffracted Kikuchi patterns [41,42]. The carbon-manganese enriched M–A microconstituents in ferrite–bainite structure was approximately 9% in the controlled rolled sample D. Fig. 4 shows the phase maps of sample D obtained from the EBSD data, confirming the presence of fine untransformed M–A constituents.

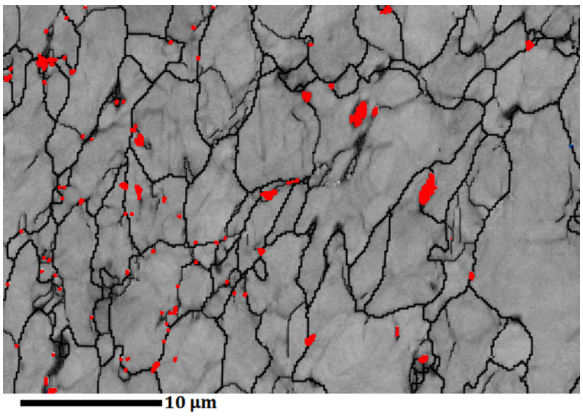

Fig. 4 – Distribution of M–A constituents (red) in ferritic matrix.

Thus, a minor fraction of austenite with higher carbon and manganese contents can be developed at lower intercritical temperatures (<750 °C), leading to the formation of stable M–A in this sample.

3.2. *Macrotexture studies*

It is believed that the crystallographic textures formed during manufacturing processing play a significant role in the mechanical behavior by providing sufficient slip systems to enhance deformation. Fig. 5 shows the normalized cubic-orthorhombic ODFs of the investigated specimens in the $Q_2 = 45^\circ$ sections of Euler space. Although the texture in HSLA steel is typically weak, the resulting crystallographic textures of samples with different start and finish rolling temperatures are dissimilar. As can be observed in Fig. 5a, b, and c, the undesirable cleavage (001)⟨110⟩ rotated cube components were characterized in the as-received sample and samples A and B, respectively. In BCC structure, the {001} plane has the smallest interplanar spacing. Therefore, this kind of crystals has the lowest dislocation mobility. In addition, the lack of adequate slip systems in {001} grains and the low dislocation mobility can lead to increases in the dislocation accumulation and stored energy. The energy increase due to dislocation accumulation leads to early fracture. Engler et al. [43] showed that the rotated cube components generated from recrystallized austenite grains followed by ferrite transformation faces are inclined at 45° in the rolling direction, which may cause shear stress and lower resistance against crack propagation. The presence of these components in sample B, which was subjected to rolling at a lower temperature of the calculated T_{NR}, revealed that the recrystallization temperature decreases with increasing deformation. Consequently, low mechanical properties can be expected in these samples due to the presence of a higher number of {001} grains in the final microstructure.

The increase in the fraction of {110} grains in samples C, D, and E can be explained by the shear deformation caused by the friction between the rolls and the plate surface [43,44]. However, the presence of {110} is common during hot rolling of HSLA steels. The rotated cube components changed to (001)⟨120⟩ components in the same plane parallel to the rolling plane in sample C. The development of a high number of {111} and {110} grains parallel to the normal direction (//ND) corresponds to the close-packed planes, which can provide adequate slip systems to contribute to plastic deformation. However, the formation of rotated cube (001)[1$\bar{1}$0] and rotated Goss (110)[1$\bar{1}$0] orientations could decrease the tensile properties and formability due to undesirably high anisotropy levels.

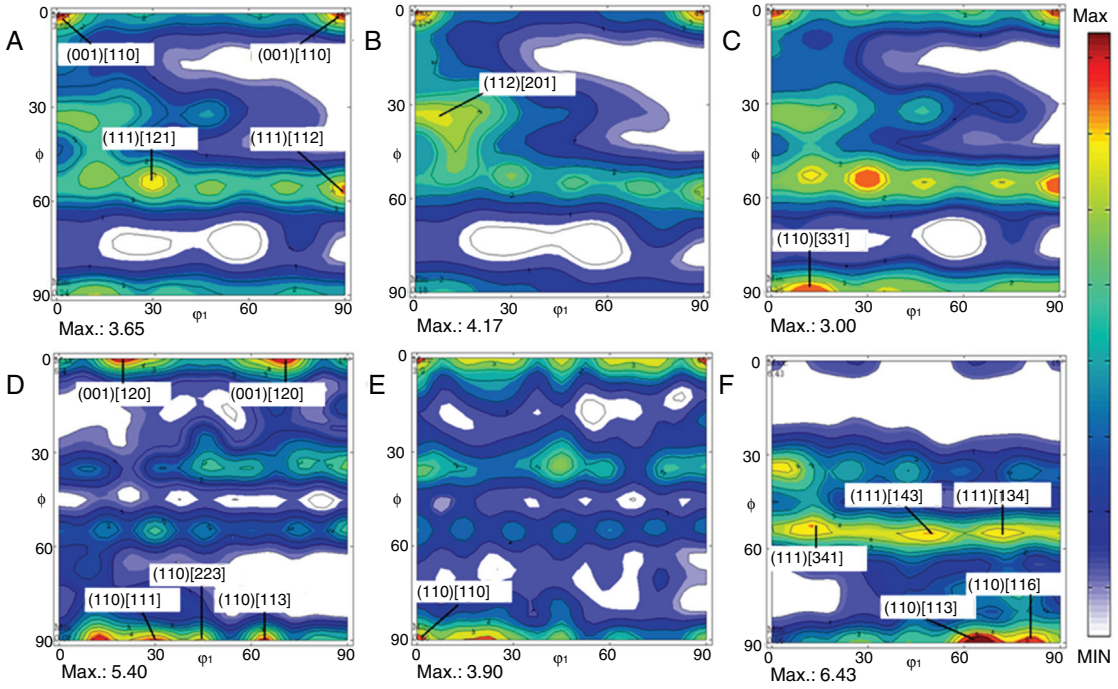

Fig. 5 – Normalized ODFs of the investigated samples in constant $\varphi 2 = 45^\circ$ sections: (a) as-received, (b) sample A, (c) sample B, (d) sample C, (e) sample D, and (f) sample E.

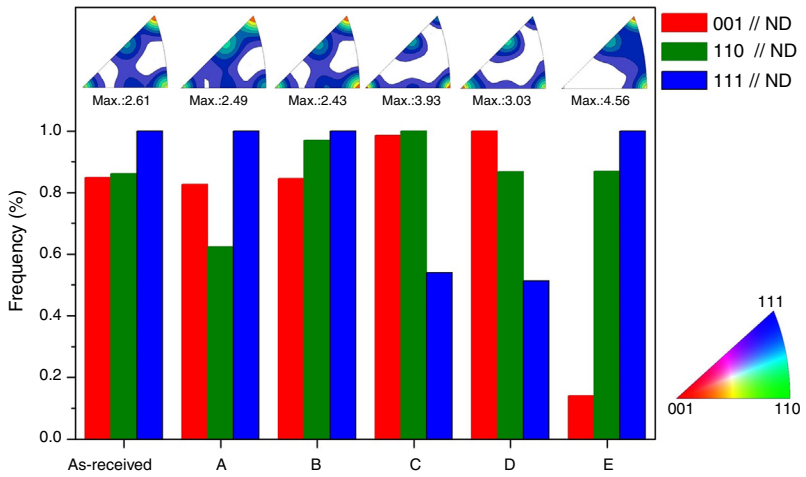

Fig. 6 – Quantitative normal friction of grains lying on the main BCC planes ({001}, {110}, and {111}) of investigated specimens. The letters A to E correspond to the types of thermomechanical processing (refer to Fig. 1).

Finally, in sample E (Fig. 5f), {001} the grains have been completely consumed and newly developed grains oriented along {110} a normal direction with about 10° deviation from the ideal Goss texture. It has been shown that the greater ductility and fracture toughness achieved when {110} planes as the principal slip planes of the BCC structures are predominant in the material [45,46].

In fact, according to Sainath [19,47] and Blondé [17], each crystal orientation has different mechanical properties at a specific external force as a result of providing enough slip systems to facilitate dislocation motion. In this manner, the close-packed {011} and {111} planes in BCC structure require minimum shear stress to begin plastic deformation or slip. Non-close-packed, low dislocation mobility {001} planes provide preferred sites for the occurrence of crystallographic defects. Fig. 6 presents the quantitative normal friction of grains lying on the main BCC planes (such as {001}, {110}, and {111}) with deviation of less than 2.5° based on the normal direction inverse pole figure of specimens. It is clearly shown that sample E, which has the lowest intensity of {001} planes and highest fraction of {111} and {110} planes, is expected to have superior tensile properties.

3.3. *Microtexture studies*

The macrotexture study conducted using XRD characterizes the overall crystal orientation distribution of bulk materials, whereas EBSD provides the local grain orientation by a statistical method (called kernel density estimation) from Kikuchi backscatter diffraction patterns [48–50]. Normal direction orientation image coloring maps (OIM) indicating the crystallographic direction parallel to the normal direction (ND) of the planes are presented in Fig. 7. High-angle boundaries (HABs), with point-to-point misorientation between two grains greater than 15°, and low angle boundaries (LABs), with a misorientation of less than 15°, are shown by thick and thin lines, respectively. As expected, the refined ferritic structure and elongated grains were observed in samples subjected to the different rolling temperatures (Fig. 7b–f). An alternative technique for grain size measurement using the linear intercept technique from optical or SEM images relies on the accuracy of the EBSD maps. Grain size was defined using a grain-boundary threshold angle of 15°. The average grain size of the as-received material was determined to be about $6.25 \pm 0.25\,\mu m$. The ferrite grain sizes were reduced under controlled rolling process in austenite region below non-recrystallization temperature to about $5.75 \pm 0.25\,\mu m$ in sample B. The continuous decreasing of the ferrite grain sizes was observed with decreasing finish rolling temperatures. The result showed that grain sizes reduced to approximately $3.25 \pm 0.25\,\mu m$ in sample D when rolling was performed at intercritical ($\alpha + \gamma$) region, suggesting that, dislocations generated by rolling were rearranged at dislocation walls and subgrain cells, provoking the subgrain rotations to form a new set of ultra-fine grains. The histograms of grain sizes in all rolled samples are presented in Fig. 8a. The decrease of rolling temperature led to the formation of pancaked prior austenite grains with high dislocation densities and resulted in an increase in the number of preferred sites for ferrite nucleation. Thus, a considerable number of ultra-fine grains with sizes smaller than $2\,\mu m$ were developed in samples C, D, and E with fractions of about 35.8, 47.7, and 44.9%, respectively.

Grain boundaries have a significant influence on the mechanical properties because they act as an impediment to dislocation movement. As a consequence, the different orientations of grains and the discontinuity of slip planes from one grain to another result in increased strength [27]. The histograms of ferrite grain boundary distributions are also presented in Fig. 8b. Although rolling at lower temperatures decreased the average grain-size distribution, no significant changes were observed in the boundary types. In samples A and B, which were rolled at higher temperatures (just above and below T_{NR}), the dislocation densities were decreased by the formation of strain-free recrystallized grains. Although the EBSD technique cannot calculate dislocation densities directly, it can evaluate their consequences by analyzing the spatial orientation changes in an individual grain because of dislocation accumulation. A new set of ultra-fine grain sizes

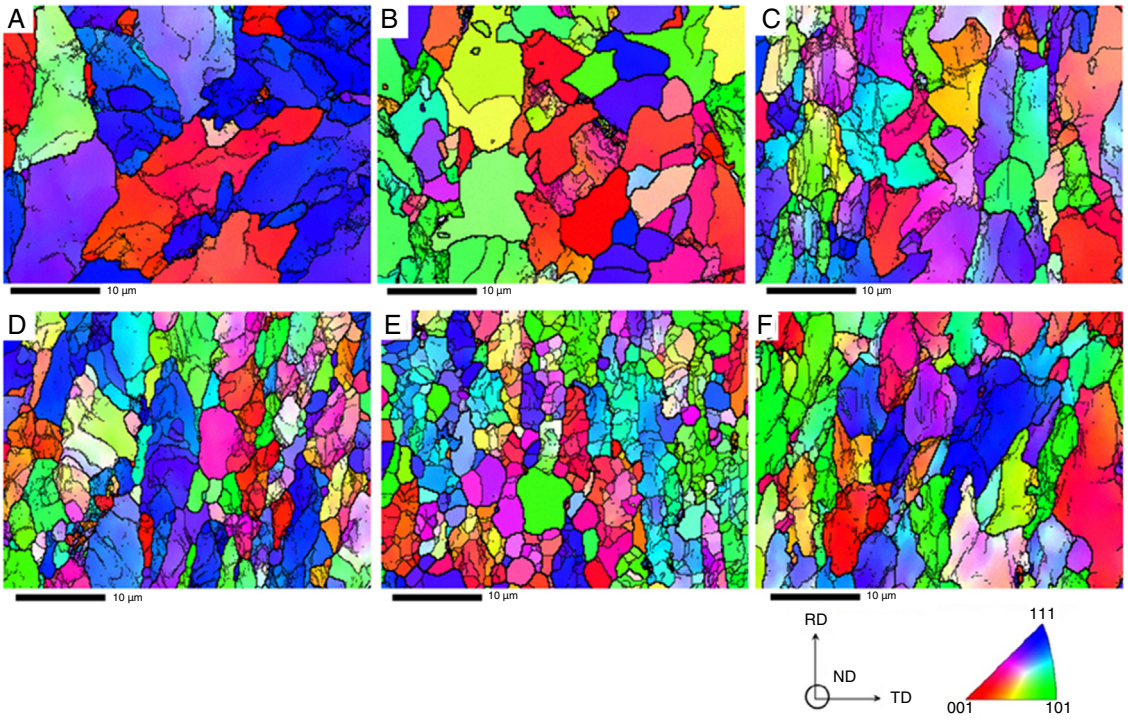

Fig. 7 – OIM maps obtained by EBSD of: (a) as-received sample; (b)–(f) samples A to E, respectively. Thick and thin lines indicate HABs and LABs, respectively.

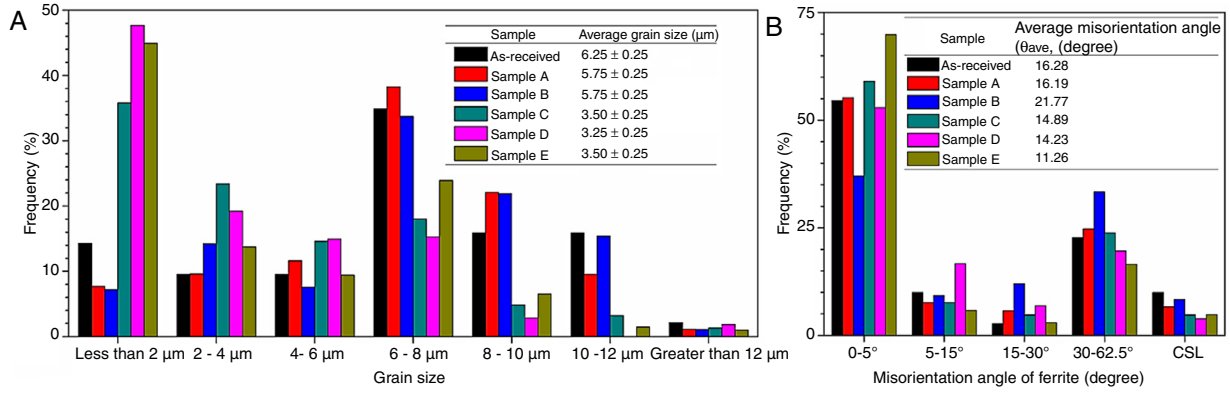

Fig. 8 – Histograms showing the frequency distributions as a function of: (a) grain size and (b) misorientation angle of ferrite.

(less than 2 μm) obtained in samples C, D, and E resulted from the gradual subgrain rotation due to increases in the dislocation densities. This is in good agreement with the results of Grilli et al. [51] and can be explained by the efficiency of dislocation annihilation by the formation of new HABs originating from dislocation walls and subgrains. In addition, the decrease in the rolling temperatures led to a reduction in dislocation annihilation due to the reduction of dislocation mobility. As a consequence, a high fraction of LABs with low grain distortion were formed in these samples (Fig. 8b). In sample B, the high value of the average misorientation angle (21.77°) can be attributed to the formation of a high fraction of strain-free recrystallized grains with a low number of dislocation densities. The highest percentage of LABs belonged to sample D, as a result of higher lattice distortion generated by the deformation at a lower temperature.

3.4. *Uniaxial tensile test*

The uniaxial tensile test was carried out at room temperature for all samples and the engineering stress–strain curves are shown in Fig. 9. It is observed that the as-received steel and the sample subjected to rolling at the higher non-recrystallization temperature (sample A) showed both the lowest tensile strength of about 611 MPa and the lowest total elongation of 12.8%, whereas an excellent combination of tensile strength and elongation was obtained in the samples that were rolled at a lower T_{NR} temperature (i.e., samples B, C, and E). The detailed mechanical properties of all samples are listed in Table 3. According to the SAE standard [52], the minimum acceptable yield stress, ultimate tensile strength, and elongation for the SAE 970X steel are 485 MPa, 585 MPa, and 15%, respectively. Accordingly, only sample D could not

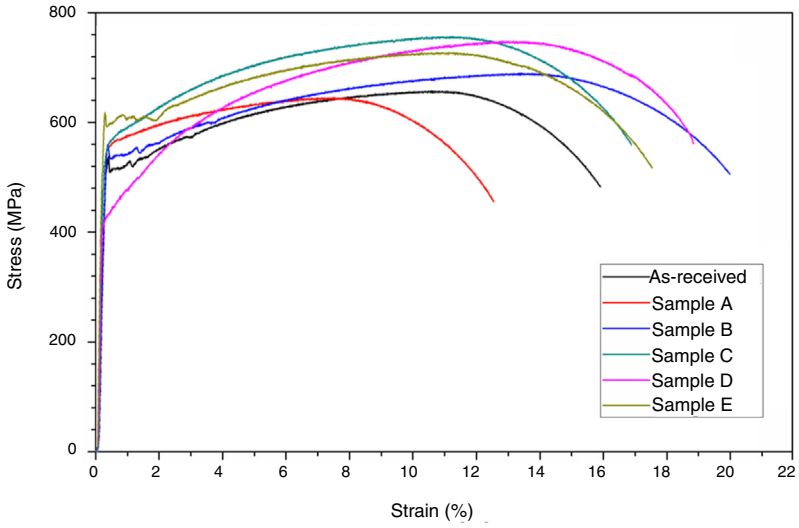

Fig. 9 – Engineering stress–strain curves for the investigated samples.

Table 3 – Tensile mechanical properties of processed specimens.

	Yield stress (MPa)	Tensile strength (MPa)	Uniform elongation (%)	Total elongation (%)	Yield/tensile ratio (YS/UTS)	Toughness ($J\,m^{-3}$)
As-received	511	615	11.6	16.3	0.83	9676
Sample A	548	611	8.1	12.8	0.90	8816
Sample B	538	637	14.0	20.3	0.84	9736
Sample C	553	713	11.5	17.4	0.77	10 750
Sample D	423	698	12.9	19.2	0.61	11 690
Sample E	594	682	11.6	17.9	0.87	12 636

meet the yield stress standard requirement. This could be related to the presence of M–A microconstituents and the formation of highly deformed undesired {001} ferrite grains as a result of the finish rolling temperature in the intercritical ($\alpha+\gamma$) field. However, the ultimate tensile strength in this sample reached approximately 697 MPa due to the formation of ultra-fine grains, which hindered dislocation movement and dislocation interaction. Conversely, the other samples that were rolled in the range of T_{NR} and Ar_3 (samples B, C, and E) successfully met the requirements specified for SAE 970X steel.

Furthermore, the ratio of yield strength to ultimate tensile strength (YS/UTS) indicates the ability to plastically deform before failure to prevent sudden rupture. The lower YS/UTS ratio in samples C and D indicates the higher resistance to deformation provided by yielding to plastic instability [53,54]. Meanwhile, the increase of the YS/UTS ratio in the other samples suggests an increase in the uniform plastic deformation ability in response to applied force and the strain hardening capacity. This resulted in the occurrence of hardening mechanisms such as solid solution strengthening, precipitation hardening, grain boundary strengthening, and transformation induced plasticity (TRIP) effects. In addition, the serrated flow characterized under plastic deformation with Lüders bands was enforced by micromechanical hardening and softening. The Lüders bands are characterized by pile-ups of mobile dislocations due to local stress concentrations in the vicinity of grain and/or phase boundaries, since a softening localized plastic deformation occurs when a high density of mobile dislocations passes through the barriers. The formation of Lüders bands during plastic deformation is common in ultrafine-grained steel [13].

The amount of energy absorbed per unit volume (toughness) calculated from the numerical integration of tensile data of measured stress–strain curves is also listed in Table 3. Factors such as microstructure, second-phase particles distribution, TRIP effect of retained austenite, and grain orientation influence the tensile mechanical properties and energy absorbed. In sample E, the combination of fine ferrite grain sizes, degenerated pearlite, distribution of M–A constituents, low stored energy (low average misorientation, Fig. 8b), and formation of {111} grains with the highest Young's modulus and yield stress [17,19] resulted in a superior toughness value among all specimens. This demonstrates that the controlled rolling temperatures could improve the toughness of the steel.

3.5. *Equibiaxial tension behavior*

The Erichsen-like cupping test is widely used in automotive industry because it is a simple method of estimating the sheet formability, where the stretchability can be determined as the resistance of localized necking [55,56]. It is known that microstructural features and crystallographic texture control

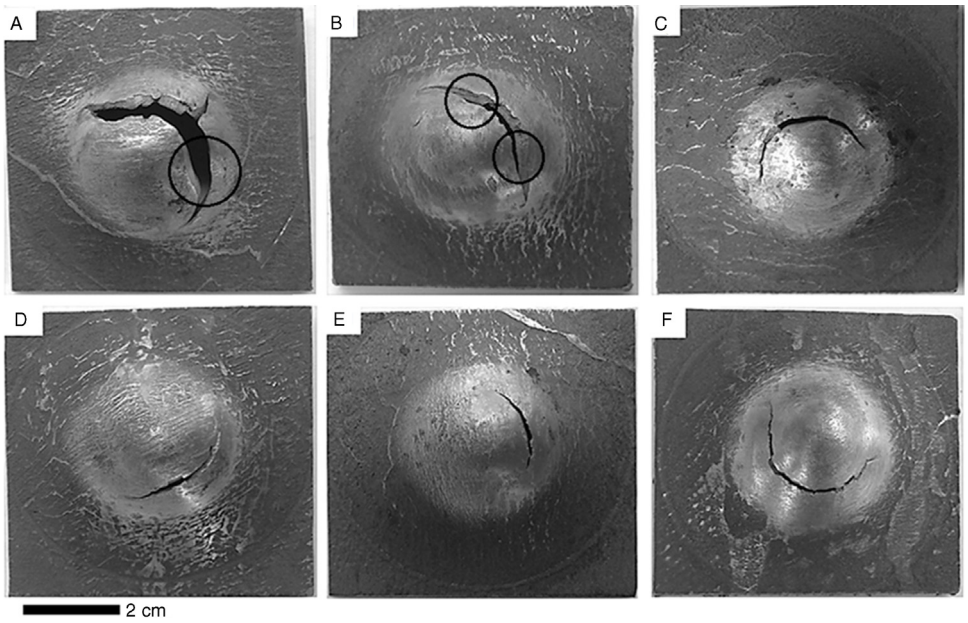

Fig. 10 – Photographs of dome free surface appearance of Erichsen tested samples: (a) as-received sample, (b) sample A, (c) sample B, (d) sample C, (e) sample D, and (f) sample E.

Table 4 – Variation in thickness of the domes on the cross-sections of Erichsen tested samples.

Sample	Dome height (mm)	Initial thickness (mm)	a		b		c	
			Thickness (mm)	Strain (%)	Thickness (mm)	Strain (%)	Thickness (mm)	Strain (%)
As-received	14.87	5.00	4.23	16.63	4.09	20.14	4.02	21.94
Sample A	15.22		4.31	14.92	3.87	25.64	3.94	23.77
Sample B	17.56		4.02	21.94	3.58	33.49	3.36	39.81
Sample C	20.07		4.31	14.92	3.07	48.91	3.14	46.55
Sample D	18.46		4.23	16.63	3.55	34.25	3.75	28.77
Sample E	21.88		3.58	33.49	3.29	42.01	2.99	51.32

the orientation-dependent (anisotropy) mechanical properties. Photographs of the Erichsen tests (in top view) of the investigated specimens after fracture are shown in Fig. 10. The fracture path of samples, which follows a crescent-shaped path around the center of the dome, is very similar for all specimens. The orange-peel effect is present in all investigated samples. Although some studies [11–13,57,58] have suggested a relationship between grain size and the orange-peel effect, no evidence was found in the current study. As a result, crystallographic texture plays a significant role in determining formability. Changes in dome height and thickness along the centerline of the dome created by the Erichsen test can help us find a correlation between crystallographic orientations and the formability limit. The dome height of samples and the variation in thickness of the domes on the cross-sections of the Erichsen tested samples were measured and are listed in Table 4. The as-received sample, which had been subjected to industrial manufacturing, and sample A showed inferior dome heights. The best formability belonged to sample E, which was isothermally rolled at 850 °C in the intercritical region. From the literature [17–19,59], {001} grains with a lack of adequate slip systems cause the early fracture. Grains lying on {110} planes parallel to the shear plane show a dual behavior. On the one hand, these grains can enhance ductility by facilitating dislocation glide. On the other hand, the shear fracture can begin by micro-void coalescence with the presence of local shear bands, leading to early fracture. Besides, the development of {110} and {111}//ND, which offered a significant benefit with regard to controlling the anisotropy and minimizing the undesired {001} grains, resulted in the excellent dome height in sample E.

Furthermore, to evaluate the uniform deformation through the thickness straining, the maximum thicknesses in three different regions, that is, the top region of the dome shape 'a' and punch displacement at points 'b' and 'c', were measured and are reported in Table 4. The least uniform deformation took place in the top region of the dome shape due to the friction effect between the punch and sample surfaces. However, the maximum deformation is obtained in the cup wall due to the plane strain stress. A detailed strain calculation at three points demonstrated that the sample E had the best formability before necking and fracture.

In the present work, different analyzing methods have been performed to propose the best thermomechanical rolling

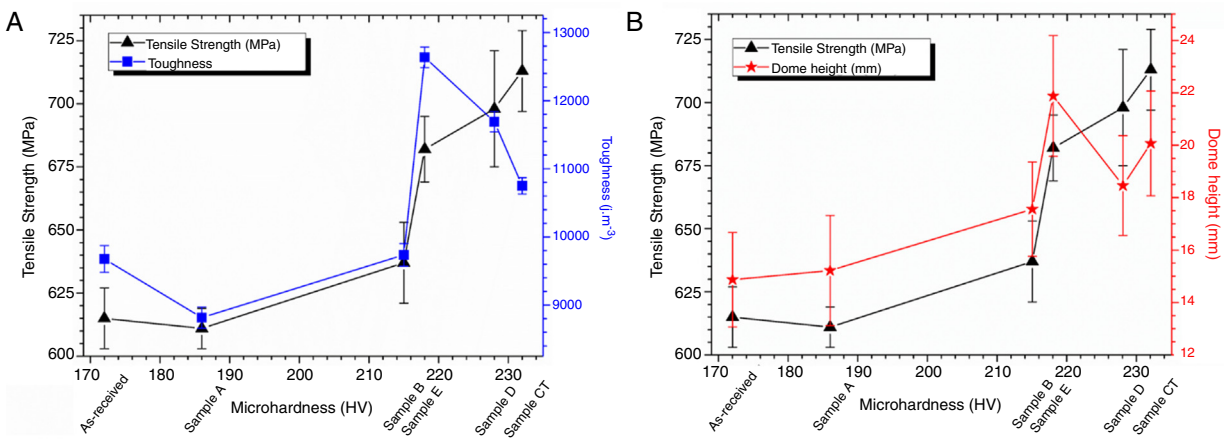

Fig. 11 – Variation of (a) tensile strength – toughness and (b) tensile strength – dome height value as a function of hardness changes of studied samples.

processing for automotive application. This included: (i) morphology, microstructure, and grain size analysis using SEM and their effects on hardness variation; (ii) grain orientation and distribution of boundary type to promote/obstruct dislocation movements, modifying plastic deformation behavior; and (iii) uniaxial and biaxial tension tests to validate formability and stretchability of resulted specimens. The variation of tensile strength, toughness (obtained from the area under stress-strain curve), and dome height as a function of hardness changes of investigated samples are shown in Fig. 11a and b. Fig. 11b shows that continuous increasing of tensile strength was accompanied with a hardness increment of investigated specimens. As a conclusion, results demonstrated that a great combination of ductility, toughness, and formability was obtained by isothermal rolling at 850 °C (sample E). The formation of low-stored-energy fine ferrite grains, along with the development of low stored energy {110} and {111} grains with adequate slip planes, prevented dislocation accumulation and localized deformation.

4. Conclusions

In summary, different controlled rolling processes (i.e., diverse start and finish rolling temperatures) were analyzed to improve the tensile mechanical properties and formability by controlling the microstructure and crystallographic textures. From the results, the following conclusions can be drawn:

- The best combination of tensile strength and elongation was achieved in the sample subjected to isothermal rolling at 850 °C (sample E).
- Sample E showed a 47% improvement of the Erichsen index compared with the as-received sample condition.
- Meaningful improvement in mechanical properties and formability (Sample E) can be obtained by the formation of ultrafine ferrite grains oriented along {011} and {111} //ND accompanied with dispersion of M–A microconstituents in the ferritic structure.

Conflicts of interest

The authors declare no conflicts of interest.

Acknowledgements

The authors acknowledge the Brazilian research agencies CNPq and CAPES, the research board of the Federal University of Ceará for the financial support and Laboratório de Caracterização de Materiais (LACAM), The Analytical Center (CT-INFRA/MCTI-SISNAD) for the provision of research facilities of this work and to Group Materiales de Ingeniería (GIMI) – Facultad de Tecnología Mecánica, Universidad Tecnológica de Pereira (UTP).

REFERENCES

[1] ASM International. High-strength low-alloy steels. In: ASM Handbook, editor. High-strength structural and high-strength low-alloy steels, properties and selection: irons, steels, and high-performance alloys. ASM International; 2001. p. 193–202.
[2] Wang LM, Du T, Lu XL, Le KX. Study of behaviors and application of micro-rare earth elements in steel. Chin Rare Earths 2001;22:37–40.
[3] Medina SF. From heterogeneous to homogeneous nucleation for precipitation in austenite of microalloyed steels. Acta Mater 2015;84:202–7, http://dx.doi.org/10.1016/j.actamat.2014.10.056.
[4] Zhang J, Ding H, Misra RDK, Wang C. Microstructural evolution and consequent strengthening through niobium-microalloying in a low carbon quenched and partitioned steel. Mater Sci Eng A 2015;641:242–8, http://dx.doi.org/10.1016/j.msea.2015.06.050.
[5] Skobir DA. High-strength low-alloy (HSLA) steels. Mater Technol 2011;45:295–301, http://dx.doi.org/10.1126/science.208.4446.862.
[6] Kurra S, Regalla SP. Experimental and numerical studies on formability of extra-deep drawing steel in incremental sheet

metal forming. J Mater Res Technol 2014;3:158–71, http://dx.doi.org/10.1016/j.jmrt.2014.03.009.
[7] Gong P, Palmiere EJ, Rainforth WM. Dissolution and precipitation behaviour in steels microalloyed with niobium during thermomechanical processing. Acta Mater 2015;97:392–403, http://dx.doi.org/10.1016/j.actamat.2015.06.057.
[8] Pan T, Chai XY, Wang JG, Su H, Yang CF. Precipitation behavior of V–N microalloyed steels during normalizing. J Iron Steel Res Int 2015;22:1037–42, http://dx.doi.org/10.1016/S1006-706X(15)30109-6.
[9] Klinkenberg C, Hulka K, Bleck W. Niobium carbide precipitation in microalloyed steel. Steel Res Int 2004;75:744–52, http://dx.doi.org/10.1002/srin.200405837.
[10] Karmakar A, Mukherjee S, Kundu S, Srivastava D, Mitra R, Chakrabarti D. Effect of composition and isothermal holding temperature on the precipitation hardening in Vanadium-microalloyed steels. Mater Charact 2017;132:31–40, http://dx.doi.org/10.1016/j.matchar.2017.08.003.
[11] Majta J, Muszka K. Mechanical properties of ultra fine-grained HSLA and Ti-IF steels. Mater Sci Eng A 2007;464:186–91, http://dx.doi.org/10.1016/j.msea.2007.01.135.
[12] Sato K, Hasimoto K, Yoshida H. Material properties and evaluation of formability of thick sheet steel for sheet forging. Nippon Steel Technical Report No. 103; 2013.
[13] Song R, Ponge D, Raabe D, Speer JG, Matlock DK. Overview of processing, microstructure and mechanical properties of ultrafine grained bcc steels. Mater Sci Eng A 2006;441:1–17, http://dx.doi.org/10.1016/j.msea.2006.08.095.
[14] Čížek J, Janeček M, Krajňák T, Stráská J, Hruška P, Gubicza J, et al. Structural characterization of ultra fi ne-grained interstitial-free steel prepared by severe plastic deformation. Acta Mater 2016;105:258–72, http://dx.doi.org/10.1016/j.actamat.2015.12.039.
[15] Quan G, Zhao L, Chen T, Wang Y, Mao Y, Lv W, et al. Identification for the optimal working parameters of as-extruded 42CrMo high-strength steel from a large range of strain, strain rate and temperature. Mater Sci Eng A 2012;538:364–73, http://dx.doi.org/10.1016/j.msea.2012.01.062.
[16] Choi P, Herbig M, Zaefferer S, Raabe D. Strain hardening by dynamic slip band re fi nement in a high-Mn lightweight steel. Acta Mater 2016;116:188–99, http://dx.doi.org/10.1016/j.actamat.2016.06.037.
[17] Blondé R, Jimenez-Melero E, Zhao L, Wright JP, Brück E, Van Der Zwaag S, et al. High-energy X-ray diffraction study on the temperature-dependent mechanical stability of retained austenite in low-alloyed TRIP steels. Acta Mater 2012;60:565–77, http://dx.doi.org/10.1016/j.actamat.2011.10.019.
[18] Rohith P, Sainath G, Choudhary BK. Molecular dynamics simulation studies on the influence of aspect ratio on tensile deformation and failure behaviour of ⟨1 0 0⟩ copper nanowires. Comput Mater Sci 2017;138:34–41, http://dx.doi.org/10.1016/j.commatsci.2017.06.019.
[19] Sainath G, Choudhary BK. Orientation dependent deformation behaviour of BCC iron nanowires. Comput Mater Sci 2016;111:406–15, http://dx.doi.org/10.1016/j.commatsci.2015.09.055.
[20] Ghosh A, Kundu S, Chakrabarti D. Effect of crystallographic texture on the cleavage fracture mechanism and effective grain size of ferritic steel. Scr Mater 2014;81:8–11, http://dx.doi.org/10.1016/j.scriptamat.2014.02.007.
[21] Zhong H, Rometsch PA, Zhu Q, Cao L, Estrin Y. Effect of pre-ageing on dynamic strain ageing in Al–Mg–Si alloys. Mater Sci Eng A 2017;687:323–31.
[22] Cancio MJ, Echaniz G, Perez TE. Characterisation of microalloy precipitates in the austenitic range of high strength low alloy steels. Steel Res 2002;73:340–6.
[23] Barbosa R, Boratto F, Yue S, Jonas JJ. The influence of chemical composition on the recrystallisation behaviour of microalloyed steels. In: Process microstruct prop HSLA steels; 1988. p. 51–61. United States.
[24] Ouchi C, Sampei T, Kozasu I. The the effect of hot rolling condition and chemical on the onset temperature of γ–α transformation after hot rolling. Trans ISIJ 1982;22:214–22.
[25] Bachmann F, Hielscher R, Schaeben H. Grain detection from 2d and 3d EBSD data — specification of the MTEX algorithm. Ultramicroscopy 2011;111:1720–33, http://dx.doi.org/10.1016/j.ultramic.2011.08.002.
[26] Bachmann F, Hielscher R, Jupp P, Pantleon W, Schaeben H, Wegert E. Inferential statistics of electron backscatter diffraction data from within individual crystalline grains. J Appl Crystallogr 2010;43:1338–55.
[27] Bunge HJ. Texture analysis in materials science. In: Mathematical methods. Elsevier Ltd.; 1969. p. 42–6.
[28] Saray O, Purcek G, Karaman I, Maier HJ. Improvement of formability of ultrafine-grained materials by post-SPD annealing. Mater Sci Eng A 2014;619:119–28, http://dx.doi.org/10.1016/j.msea.2014.09.016.
[29] Foecke T, Gnaeupel-Herold T. Robustness of the sheet metal springback cup test. Metall Mater Trans A: Phys Metall Mater Sci 2006;37:3503–10, http://dx.doi.org/10.1007/s11661-006-1045-3.
[30] Yang J, Liu Q, Sun D, Li X. Microstructure and transformation characteristics of acicular ferrite in high niobium-bearing microalloyed steel. J Iron Steel Res Int 2010;17:53–9, http://dx.doi.org/10.1016/S1006-706X(10)60114-8.
[31] Silva RDA, Souza LFG, Morales EV, Rios PR, Bott IDS. Formation of microphases and constituents from remaining austenite decomposition in API X80 steel under different processing conditions. Mater Res 2015;18:908–17, http://dx.doi.org/10.1590/1516-1439.315214.
[32] Yamane T, Hisayuki K, Kawazu Y, Takahashi T, Kimura Y, Tsukuda S. Improvement of toughness of low carbon steels containing nitrogen by fine microstructures. J Mater Sci 2002;37:3875–9, http://dx.doi.org/10.1023/A:1019695104094.
[33] Medina SF, Ruiz-bustinza I, Robla J, Calvo J. Theoretical and experimental nucleation and growth of precipitates in a medium carbon–vanadium steel. Metals 2017;7:178–88, http://dx.doi.org/10.3390/met7020045.
[34] Wang Y, Chen M, Zhou F, Ma E. High tensile ductility in a nanostructured metal. Nature 2002;419:912–5, http://dx.doi.org/10.1038/nature01133.
[35] Wang TS, Li Z, Zhang B, Zhang XJ, Deng JM, Zhang FC. High tensile ductility and high strength in ultrafine-grained low-carbon steel. Mater Sci Eng A 2010;527:2798–801, http://dx.doi.org/10.1016/j.msea.2010.01.072.
[36] Hippchen P, Lipp A, Grass H, Craighero P, Fleischer M, Merklein M. Modelling kinetics of phase transformation for the indirect hot stamping process to focus on car body parts with tailored properties. J Mater Process Technol 2016;228:59–67.
[37] Bhadeshia HKDH. Proceedings of the international seminar on welding of high strength pipeline steels, CBMM and the minerals. Metals Mater Soc 2013:99–106.
[38] Hrivnak I, Matsuda F, Li Z, Ikeuchi K, Okada H. Investigation of metallography and behavior of M–A constituent in weld HAZ of HSLA steels. Trans JWRI 1992;21:241–53.
[39] Matsuda F, Ikeuchi K, Fukada Y, Horii Y, Okada H, Shiwaku T, et al. M–A constituent in welded metallurgical joint in Japan. Trans JWRI 1995;24:1–24.
[40] You Y, Shang C, Chen L, Subramanian S. Investigation on the crystallography of the transformation products of reverted

austenite in intercritically reheated coarse grained heat affected zone. Mater Des 2013;43:485–91, http://dx.doi.org/10.1016/j.matdes.2012.07.015.
[41] Nowell MM, Wright S. Phase differentiation via combined EBSD and XEDS. J Microsc 2004;213:296–305.
[42] Qazi SJS, Rennie AR, Cockcroft JK, Vickers M. Use of wide-angle X-ray diffraction to measure shape and size of dispersed colloidal particles. J Colloid Interface Sci 2009;338:105–10, http://dx.doi.org/10.1016/j.jcis.2009.06.006.
[43] Engler O, Huh MY, Tome CN. A study of through-thickness texture gradients in rolled. Metall Mater Trans A 2000;31:2299–315, http://dx.doi.org/10.1007/s11661-000-0146-7.
[44] Masoumi M, Flavio L, Herculano G, Ferreira H, De Abreu G. Study of texture and microstructure evaluation of steel API 5L X70 under various thermomechanical cycles. Mater Sci Eng A 2015;639:550–8, http://dx.doi.org/10.1016/j.msea.2015.05.020.
[45] Masoumi M, De Barros IF, Flavio L, Herculano G, Livia H, Coelho F, et al. Effect of microstructure and crystallographic texture on the Charpy impact test for maraging 300 steel. Mater Charact 2016;120:203–9.
[46] Joo MS, Suh D, Bae JH, Bhadeshia HKDH. Role of delamination and crystallography on anisotropy of Charpy toughness in API-X80 steel. Mater Sci Eng A 2012;546:314–22.
[47] Sainath G, Choudhary BK. Molecular dynamics simulations on size dependent tensile deformation behaviour of [110] oriented body centred cubic iron nanowires. Mater Sci Eng 2015;640:98–105, http://dx.doi.org/10.1016/j.msea.2015.05.084.
[48] Lassen NK. Automated determination of crystal orientations from EBSPs. Technical University of Denmark; 1994. ISSN 0909-3192.
[49] Adams BL, Wright SL, Kunze K. Orientation mapping: the emergence of a new microscopy. Metall Trans A 1993;24:819–31.
[50] Wright SI, Adams BL. Automatic-analysis of electron backscatter diffraction patterns. Metall Trans A: Phys Metall Mater Sci 1992;23:759–67, http://dx.doi.org/10.1007/BF02675553.
[51] Grilli N, Janssens KGF, Nellessen J, Sandlöbes S, Raabe D. Multiple slip dislocation patterning in a dislocation-based crystal plasticity finite element method. Int J Plast 2018;100:104–21, http://dx.doi.org/10.1016/j.ijplas.2017.09.015.
[52] Automotive: SAE Technical Standards WIP, G-21 Counterfeit Materiel Committee, Procedure for Visual Evaluation of Interior and Exterior Automotive Trim; 2015.
[53] Kim YM, Kim SK, Lim YJ, Kim NJ. Effect of microstructure on the yield ratio and low temperature toughness of linepipe steels. ISIJ Int 2002;42:1571–7, http://dx.doi.org/10.2355/isijinternational.42.1571.
[54] Fan L, Zhou D, Wang T, Li S, Wang Q. Tensile properties of an acicular ferrite and martensite/austenite constituent steel with varying cooling rates. Mater Sci Eng A 2014;590:224–31, http://dx.doi.org/10.1016/j.msea.2013.10.037.
[55] Hamada AS, Kisko A, Khosravifard A, Hassan MA, Karjalainen LP, Porter D. Ductility and formability of three high-Mn TWIP steels in quasi-static and high-speed tensile and Erichsen tests. Mater Sci Eng A 2018;717:154, http://dx.doi.org/10.1016/j.msea.2018.01.092.
[56] Hosford WF, Caddell RM. Metal forming: mechanics and metallurgy. 2nd ed. Englewood Cliffs, NJ: Prentice Hall PTR; 1993.
[57] Baker TN. Processes, microstructure and properties of vanadium microalloyed steels. Mater Sci Technol 2009;25:1083–107, http://dx.doi.org/10.1179/174328409X453253.
[58] Zhang X, Fan L, Xu Y, Li J, Xiao X, Jiang L. Effect of aluminum on microstructure, mechanical properties and pitting corrosion resistance of ultra-pure 429 ferritic stainless steels. Mater Des 2015;65:682–9, http://dx.doi.org/10.1016/j.matdes.2014.09.074.
[59] Masoumi M, Silva CC, Ferreira H, De Abreu G. Effect of rolling in the recrystallization temperature region associated with a post-heat treatment on the microstructure, crystal orientation, and mechanical properties of API 5L X70 pipeline steel. Mater Res 2017;20:151–60.